An Improved Zero-Switching-Loss Inverter With Low Conduction Loss

Yun Liu, Huafeng Xiao, *Senior Member, IEEE*, Wei Hua, *Senior Member, IEEE*, and Ming Cheng, *Fellow, IEEE*

***Abstract*—Zero-switching-loss (ZSL) transformerless inverter (TLI) is beneficial for increasing switching frequency for distributed photovoltaic generation systems. However, the existing ZSL-TLIs bear high conduction loss because of the coupling between the resonance tanks and the main power loops. In order to solve this problem, an improved zero-switching-loss H6 inverter (IZSL-H6) with low conduction loss composed of novel resonance tanks and an H6 inverter has been proposed in this article. The resonance tanks provide zero-current switching (ZCS) for H6 inverter switches, and the auxiliary devices of the resonance tanks are also turned ON and OFF with ZCS. Compared with the existing ZSL-H6, IZSL-H6 reduces conduction loss by avoiding resonant current flow through the main switches during resonant capacitor charging mode and reducing the number of power devices in the main power loops during the freewheeling mode. Resonant parameters design, soft-switching criteria, and common-mode voltage characteristics are discussed. Finally, a 1000-W prototype has been developed to verify the theoretical analysis of the proposed IZSL-H6.**

***Index Terms*—Conduction loss, resonance tank, transformerless inverter (TLI), zero-switching-loss (ZSL).**

I. Introduction

In RECENT years, with the increasing demand for energy and growing environmental awareness, solar energy, as a renewable clean energy, has received widespread attention and application [1], [2], [3]. The decentralized layout of distributed photovoltaic (PV) power generation systems has the advantages of strong adaptability, flexible installation, and high reliability, which has contributed to increase the share of PV power generation applications [4], [5].

A transformerless inverter (TLI) with low cost, high efficiency, and compact size is suitable for distributed PV power generation systems [6]. The full-bridge inverter is a TLI, with the advantages of higher input voltage utilization, higher conversion efficiency, and smaller output current under unipolar sinusoidal pulsewidth modulation (SPWM) [7], [8]. However, serious safety issues arise due to the common-mode (CM) leakage current (LC) generated by parasitic capacitors between PV panels and the ground so that this kind of inverter cannot be directly equipped in PV power generation systems [9], [10]. In order to improve the LC suppression capability of unipolar SPWM full-bridge TLI, extensive research was carried out in [11], [12], [13], and [14], categorizing into dc bypass and ac bypass. For example, H6 inverter is obtained by connecting a switch in series at the positive and negative points of the dc link in a full-bridge inverter [11]. In addition, a pair of reverse series switches is added at the midpoint of the bridge leg in the full-bridge inverter to obtain the HERIC inverter [13]. This type of bypass inverter effectively reduces LC by interrupting the electrical connection between dc link and ac side and cutting off the CM loop in the freewheeling mode. However, the bypass-type inverter is unable to completely eliminate high-frequency LC due to fluctuations in CM voltage.

Based on the CM analytical model at switching frequency in [15], maintaining a constant CM voltage is an effective method to eliminate LC in full-bridge inverter with unipolar SPWM. The existing TLI with the clamp structure has shown good performance in suppressing LC under unipolar output conditions due to maintaining a constant CM voltage value in freewheeling mode [16], [17], [18], [19], [20], [21]. However, bypass-type inverters and clamp-type inverters typically employ hard-switching (HS), and the switching frequency is limited considering switching loss, resulting in an increase in filter size and cost, and a corresponding decrease in system power density.

Soft-switching technology can reduce or even eliminate switching loss, which is an important approach to improve efficiency and promote high-frequency operation [22], [23]. Resonant dc-link inverter (RDCLI) and resonant pole inverter proposed by Divan and Skibinski [24], [25] have pioneered the application of soft-switching technology in dc–ac inverters, and thus expanded a series of soft-switching inverters [26], [27], [28], [29], [30], [31], [32]. The active clamp RDCLI in [29] and [30] provides zero-voltage switching (ZVS) of the switches through an auxiliary circuit connected in series on the dc link, which reduces drain–source voltage to zero before turning ON the switches. Adding the auxiliary circuit on ac side is also a means to achieve ZVS. The soft-switching inverters proposed in [31] and [32] use the filtering inductor as the magnetic inductor

Manuscript received 15 September 2023; revised 6 December 2023; accepted 26 January 2024. Date of publication 6 February 2024; date of current version 20 March 2024. This work was supported by the 2022 Jiangsu Carbon Peak and Neutrality Technology Innovation Special Fund (Industrial Foresight and Key Core Technology Research) "Research and Development of Key Technologies for Grid Integration Operation and Control of Renewable Energy Sources" under Project BE2022003. Recommended for publication by Associate Editor B. Mirafzal. *(Corresponding author: Huafeng Xiao.)*

The authors are with the College of Electrical Engineering, Southeast University, Nanjing 210096, China, and also with the Jiangsu Provincial Key Laboratory of Smart Grid Technology and Equipment, Southeast University, Nanjing 210096, China (e-mail: lyun@seu.edu.cn; xiaohf@seu.edu.cn; huawei1978@seu.edu.cn; mcheng@seu.edu.cn).

Color versions of one or more figures in this article are available at https://doi.org/10.1109/TPEL.2024.3362854.

Digital Object Identifier 10.1109/TPEL.2024.3362854

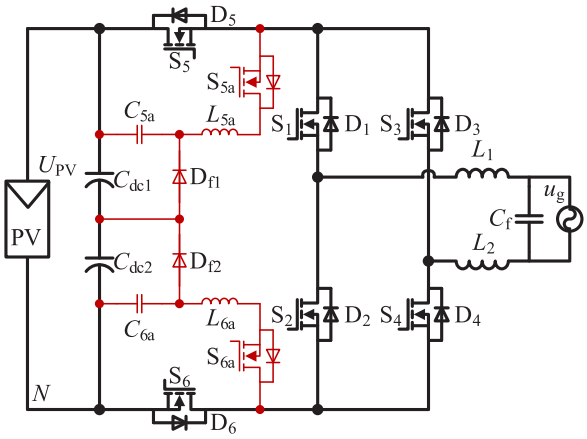

Fig. 1. ZSL-H6 inverter in [35].

and the leakage inductor as the resonant inductor, which can achieve ZVS of the main switches and zero-current switching (ZCS) of the auxiliary switches. However, the above inverters are not directly applicable to transformerless PV power generation systems, as the focus is on the implementation of soft switching and the CM voltage has not been considered. A series of novel freewheeling resonance tank inverters for TLI has been proposed by Xiao et al. [33], [34], [35]. The zero-voltage-transition (ZVT) inverter proposed in [33] achieves ZVT of the high-frequency main switches and zero-current turn-ON of the added auxiliary switches, and obtains a constant CM voltage under unipolar SPWM through the freewheeling resonance tanks. However, the auxiliary switches were hard turn-OFF. In addition, the zero-current-transition inverter proposed in [34] achieved zero-current turn-OFF of the main switches and zero-voltage turn-ON for the auxiliary switches. Addressing the issues of hard turn-ON for the main switches and reverse recovery of diodes in [34], novel resonance tanks were proposed in [35]. Zero switching loss (ZSL) of the high-frequency power devices in clamp-type hard-switching H6 (HS-H6) proposed in [17] and other full-bridge inverters can be achieved due to the application of these resonance tanks, ZSL-H6 is shown in Fig. 1. However, due to the coupling between the resonant tanks and the main power loops, the number of power devices in [35] flowing through by the resonant current is relatively large. It leads to more conduction loss and a doubling of the current amplitude of the main switches.

This article focuses on reducing the conduction loss of existing ZSL inverters by introducing a novel resonant tank in H6 to achieve ZSL. The proposed improved zero-switching-loss H6 inverter (IZSL-H6) has excellent performance in LC suppression due to the CM voltage being clamped at a constant value. Compared with ZSL-H6 in [35], IZSL-H6 effectively separates the resonance tanks and the main power loops at all stages except for the soft-switching stages. Specifically, during resonant capacitor charging mode, the resonant currents in IZSL-H6 bypass the main switches, avoiding the doubling of current amplitude and, consequently, reducing conduction loss; during the freewheeling mode, reducing the number of power devices through which the output current flows can further decrease conduction loss.

The rest of this article is organized as follows. Section II introduces the structure and operation principle of the proposed IZSL-H6. The state-plane trajectory, voltage and current stresses, and conduction loss of power devices of ZSL-H6 and IZSL-H6 are compared in Section III. Section IV analyzes the soft-switching criteria and CM characteristics. The experimental results of a 1000-W prototype are provided in Section V. Finally, Section VI concludes this article.

II. Circuit Structure and Operation Principle

The IZSL-H6 inverter is shown in Fig. 2(a). The main circuit consists of dc-link capacitors $C_{\rm dc1}$ and $C_{\rm dc2}$, main switches S_1–S_6, and output filter inductors L_1 and L_2, where $L_1 = L_2$, and a filter capacitor C_f. The resonance tanks are composed of resonant inductors L_{5a} and L_{6a}, resonant capacitors C_{5a} and C_{6a}, auxiliary switches S_{5a} and S_{6a}, freewheeling diodes D_{f1} and D_{f2}, and auxiliary diodes D_{a1} and D_{a2}, where $L_{5a} = L_{6a} = L_r$ and $C_{5a} = C_{6a} = C_r$. The modulation strategy employed by IZSL-H6 is illustrated in Fig. 2(b), where the main switches S_1 and S_4 turn ON during the positive half-cycle of the grid frequency, while the main switches S_2 and S_3 turn ON during the negative half-cycle of the grid frequency, and both the main switches S_5 and S_6 and auxiliary switches S_{5a} and S_{6a} operate at high frequency throughout the entire grid-frequency cycle. Fig. 2(c) shows the key waveforms at the switching-frequency scale. Within a complete switching cycle of the main switches S_5 and S_6, there are eight operational stages, as illustrated in Fig. 3, which depict the equivalent circuit for each stage and highlight the key features.

Stage 1 *[t_0, t_1]:* Before t_0, IZSL-H6 operates in the freewheeling mode, and the resonant current is equal to the output current, flowing through L_{5a}, L_{6a}, D_{f1}, and D_{f2}. The resonant voltages u_{C5a} and u_{C6a} across C_{5a} and C_{6a} are both zero. Refer to Fig. 3(a), at t_0, S_5 and S_6 are turned ON, and the resonant currents i_{L5a} and i_{L6a} through L_{5a} and L_{6a} decrease linearly with a constant slope. The slope is determined by the input voltage $U_{\rm PV}$ and the resonant inductance L_r. Simultaneously, the currents i_{S5} and i_{S6} through S_5 and S_6 increase at the same slope, achieving ZCS turn-ON for S_5 and S_6. At this stage

$$i_{L5a,L6a}(t) = i_{Df1,Df2}(t) = I_L - \frac{U_{\rm PV}}{2L_r}(t - t_0) \tag{1}$$

$$i_{S5,S6}(t) = \frac{U_{\rm PV}}{2L_r}(t - t_0). \tag{2}$$

Stage 2 *[t_1, t_2]:* Refer to Fig. 3(b), at t_1, the currents i_{S5} and i_{S6} rise to the amplitude I_L of the output current, while the currents i_{Df1} and i_{Df2} through D_{f1} and D_{f2} decrease to zero. Therefore, D_{f1} and D_{f2} achieve ZCS turn-OFF, effectively eliminating the reverse recovery issue. Subsequently, the inverter enters the conventional energy transfer mode. At this stage

$$i_{S5,S6}(t) = I_L. \tag{3}$$

Stage 3 *[t_2, t_3]:* Refer to Fig. 3(c), at t_2, the resonance tanks are activated due to S_{5a} and S_{6a} turning ON. The voltages u_{C5a} and u_{C6a}, as well as the currents i_{L5a} and i_{L6a}, begin to increase from zero under the action of $U_{\rm PV}$. The currents i_{S5a} and i_{S6a}

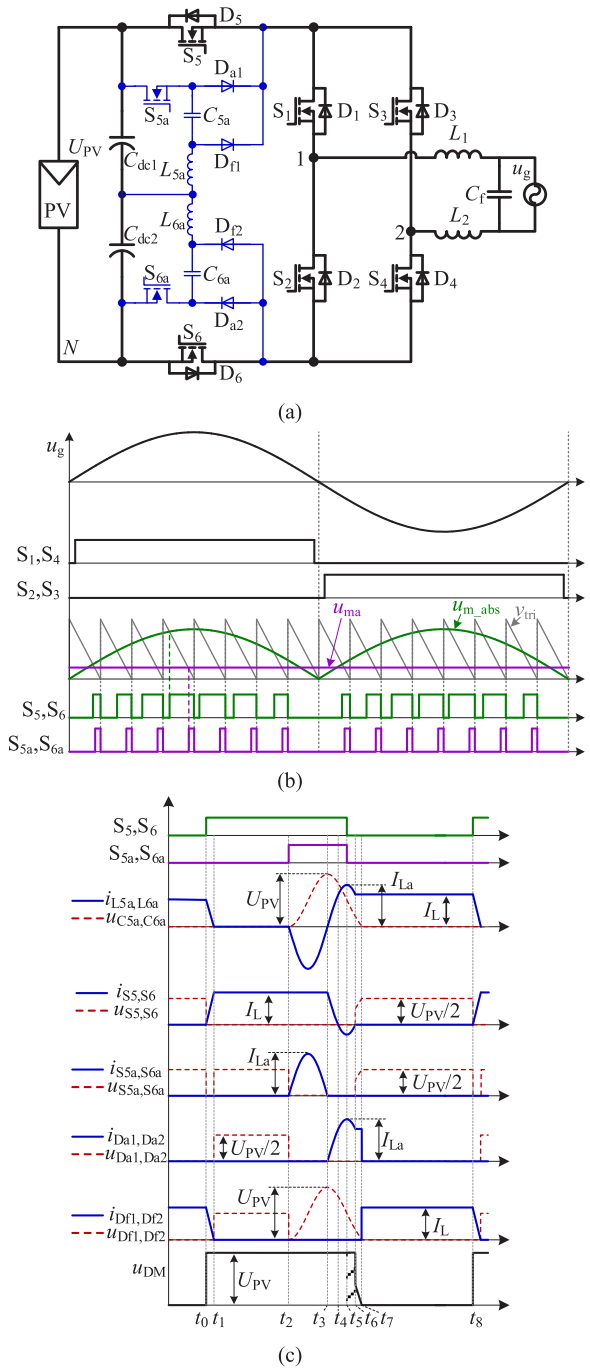

Fig. 2. Proposed IZSL-H6 inverter. (a) IZSL-H6. (b) Driving logic at the grid-frequency scale. (c) Key waveforms at the switching-frequency scale.

of S_{5a} and S_{6a} are equal to i_{L5a} and i_{L6a}, resulting in the ZCS turn-ON of S_{5a} and S_{6a}. Once i_{L5a} and i_{L6a} reach the amplitude I_{La} of the resonant current, they start to decrease. By t_3, the resonance tanks have completed half of a cycle. The voltages u_{C5a} and u_{C6a} have reached the amplitude U_{PV} of the resonant voltage, and the currents i_{L5a} and i_{L6a} have decreased to zero. S_{5a} and S_{6a} achieve ZCS turn-OFF. At this stage

$$i_{L5a,L6a}(t) = -I_{La}\sin\omega_r(t-t_2) \tag{4}$$

$$u_{C5a,C6a} = \frac{U_{PV}}{2}[1-\cos\omega_r(t-t_2)] \tag{5}$$

where $\omega_r = 1/\sqrt{L_rC_r}$ and $I_{La} = U_{PV}/2/Z_r = U_{PV}/(2\sqrt{L_r/C_r})$.

Stage 4 *[t_3, t_4]:* Refer to Fig. 3(d), at t_3, the resonance tanks enter the three-quarter cycle. The voltages u_{C5a} and u_{C6a} start decreasing from U_{PV}, while the currents i_{L5a} and i_{L6a} increase from zero. The currents of D_{a1} and D_{a2} are equal to i_{L5a} and i_{L6a}. Simultaneously, the currents i_{S5} and i_{S6} decrease from I_L due to the influence of i_{L5a} and i_{L6a}

$$i_{S5,S6}(t) = I_L - i_{L5a,L6a}(t). \tag{6}$$

Stage 5 *[t_4, t_5]:* Refer to Fig. 3(e), at t_4, the currents i_{L5a} and i_{L6a} increase to I_L and continue to rise. Once the currents i_{S5} and i_{S6} decrease to zero, the antiparallel diodes D_5 and D_6 of S_5 and S_6 begin to conduct, causing the currents i_{S5} and i_{S6} to increase from zero to the opposite direction. Meanwhile, the voltages u_{C5a} and u_{C6a} continue to decrease. By t_5, the currents i_{L5a} and i_{L6a} have reached the amplitude I_{La}. After t_4, S_5 and S_6 meet the conditions for ZCS turn-OFF.

Stage 6 *[t_5, t_6]:* Refer to Fig. 3(f), at t_5, the currents i_{S5} and i_{S6} decrease to I_L–I_{La} and then begin to increase until they reach zero at t_6. Simultaneously, the currents i_{L5a} and i_{L6a} gradually decrease from I_{La} to I_L, and the voltages u_{C5a} and u_{C6a} continue to decrease.

Stage 7 *[t_6, t_7]:* Refer to Fig. 3(g), at t_6, S_5 and S_6 are completely turned OFF. The currents i_{L5a} and i_{L6a} become equal to I_L, and the resonant capacitors C_{5a} and C_{6a} discharge through D_{a1} and D_{a2} with a discharge current of I_L. At this stage

$$i_{L5a,L6a}(t) = I_L \tag{7}$$

$$u_{C5a,C6a}(t) = \frac{U_{PV}}{2}\left[1-\cos\left(\arcsin\left(-\frac{I_L}{I_{La}}\right)\right)\right] - \frac{I_L}{C_r}(t-t_6). \tag{8}$$

Stage 8 *[t_7, t_8]:* Refer to Fig. 3(h), at t_7, the discharge of C_{5a} and C_{6a} is completed, and u_{C5a} and u_{C6a} drop to zero. D_{a1} and D_{a2} achieve ZCS turn-OFF. D_{f1} and D_{f2} enable ZCS turn-ON, providing a continuous path for the resonant current I_{La}, as well as the inverter enters the conventional freewheeling mode. Starting from t_8, a new switching cycle begins and the above operation described is repeated.

III. Comparison of ZSL-H6 and IZSL-H6

A. Comparison of State-Plane Trajectory

Taking the upper resonant tank as an example, the modes of ZSL-H6 and IZSL-H6 can be summarized, as shown in Table I. It is important to note that the order of modes in the table does not necessarily correspond to the sequence of circuit operations. From Table I, the common feature between ZSL-H6 and IZSL-H6 is achieving ZCS turn-ON and turn-OFF for the main switch S_5 by transferring the output current i_L between the resonant tank and the main power loop. Combining the state-plane trajectory in Fig. 4 and Table I, analyze in detail the performance improvements of IZSL-H6 compared with ZSL-H6.

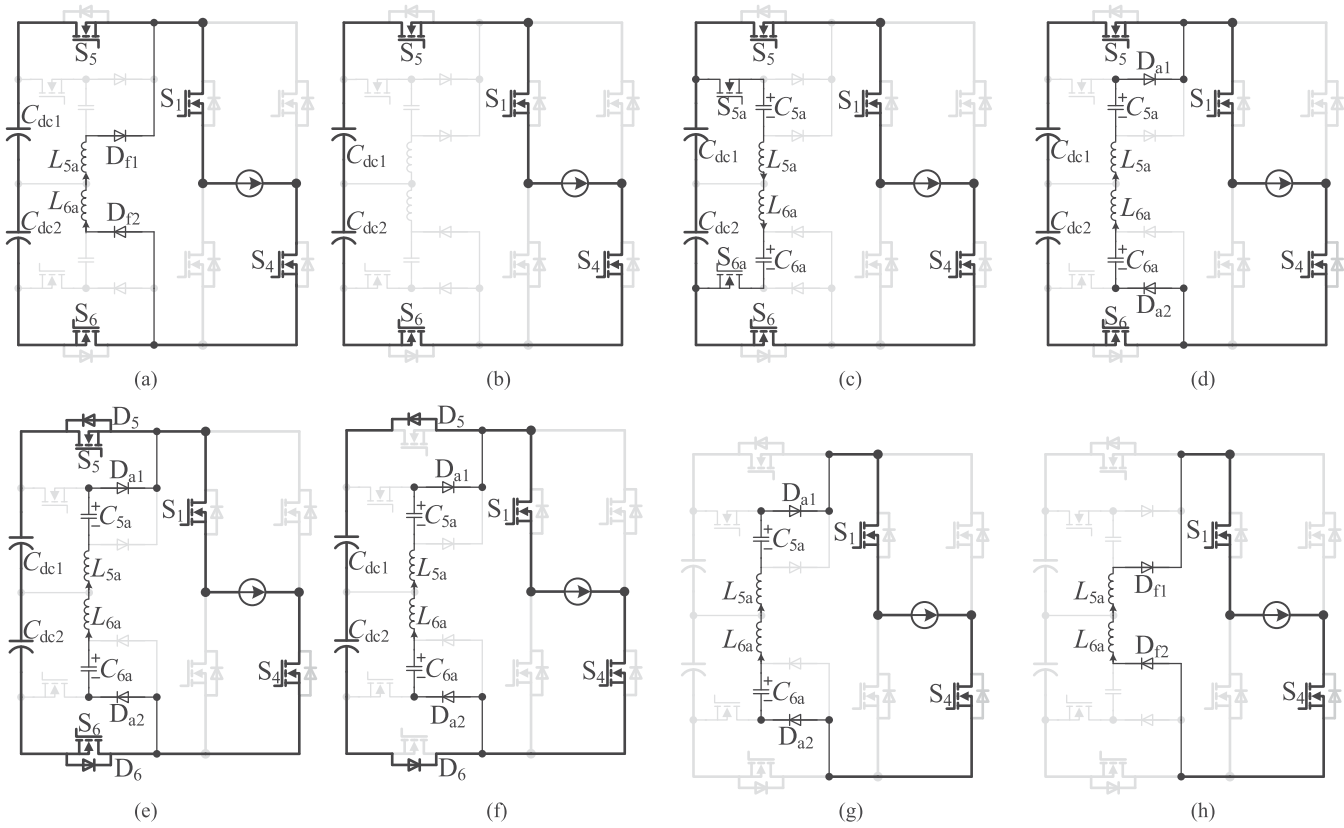

Fig. 3. Equivalent circuits in a positive half cycle. (a) Stage 1 [t_0, t_1]. (b) Stage 2 [t_1, t_2]. (c) Stage 3 [t_2, t_3]. (d) Stage 4 [t_3, t_4]. (e) Stage 5 [t_4, t_5]. (f) Stage 6 [t_5, t_6]. (g) Stage 7 [t_6, t_7]. (h) Stage 8 [t_7, t_8].

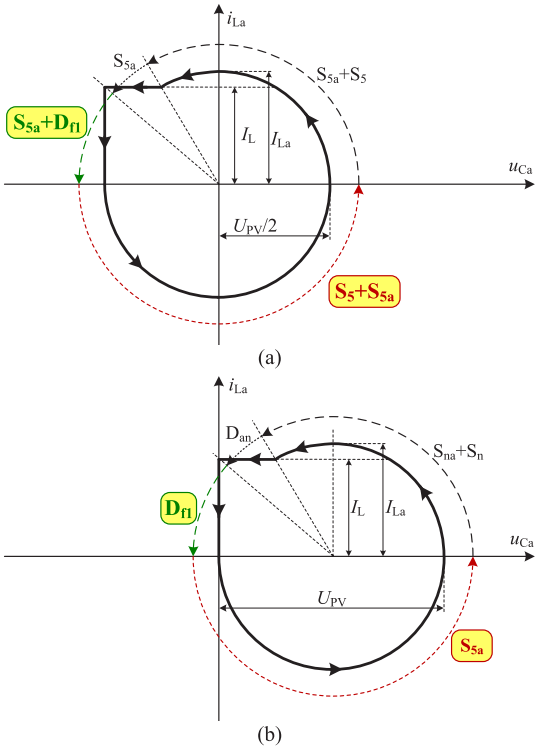

Fig. 4. State-plane trajectory. (a) State-plane trajectory of ZSL-H6 in [35]. (b) State-plane trajectory of the proposed IZSL-H6.

TABLE I
SUMMARY OF OPERATING MODES OF ZSL-H6 AND IZSL-H6

	ZSL-H6	IZSL-H6
Energy transfer mode	i_L flows through S_5. Resonance tank does not operate.	
Soft-switching mode	i_L is transferred from resonance tank to main power loop. S_5 achieves ZCS turn-on.	
Soft-switching mode	i_L is transferred from the main power loop to resonance tank.	
	S_5 ZCS turn-off. S_{5a} ZCS turn-off.	S_5 ZCS turn-off. D_{a1} ZCS turn-off.
Resonant capacitor charging mode	i_{Lr} flows through S_{5a} and S_5. S_{5a} ZCS turn-on.	i_{Lr} flows through S_{5a}. S_{5a} ZCS turn-on and turn-off.
Freewheeling mode	i_L flowing through D_{f1} and S_{5a}.	i_L flowing through D_{f1}.

1) In the resonant capacitor charging mode (the red dashed arc), the resonant current i_{Lr} flows through the auxiliary switch S_{5a} and the main switch S_5 of ZSL-H6. As a result, the current of the main switch S_5 is the sum of the output current and the resonant current. It increases the current amplitude on S_5 by at least twice the output current amplitude, thereby increasing the conduction loss. In contrast, the state-plane trajectory of IZSL-H6 demonstrates

TABLE II
COMPONENT QUANTITY AND VOLTAGE RATE

	Voltage Rating	HS-H6	ZSL-H6	IZSL-H6
Main switch	U_{PV}	4	4	4
	$U_{PV}/2$	2	2	2
Auxiliary switch	U_{PV}	0	0	0
	$U_{PV}/2$	0	2	2
Diode	U_{PV}	0	2	2
	$U_{PV}/2$	2	0	2

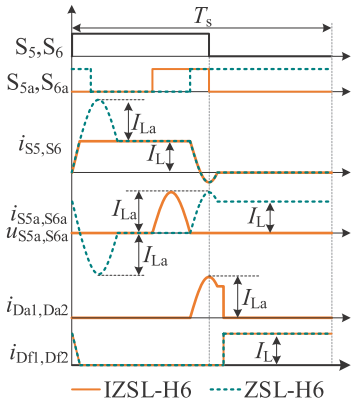

Fig. 5. Current waveforms of high-frequency semiconductor power devices of ZSL-H6 in [35] and IZSL-H6 during a switching cycle.

that the resonant current only flows through the auxiliary switch S_{5a}. The current amplitude and conduction loss of the main switch S_5 can be effectively reduced due to the approach.

2) In the freewheeling mode (the green dashed arc), the resonant current is equal to the output current, flowing through the freewheeling diode D_{f1} and the auxiliary switch S_{5a} of ZSL-H6. In contrast, the proposed state-plane trajectory indicates that the output current solely flows through the freewheeling diode D_{f1}, which can further reduce conduction loss.

B. Comparison of Voltage and Current Stresses

The comparison of power device count and voltage stress in HS-H6, ZSL-H6, and IZSL-H6 is presented in Table II. Compared with HS-H6, ZSL-H6 includes two additional switches with a voltage stress of $U_{PV}/2$ while maintaining the same number of diodes but raising the voltage stress from $U_{PV}/2$ to U_{PV}. IZSL-H6 introduces two diodes with a voltage stress of $U_{PV}/2$ compared with ZSL-H6, while the number of other devices and their respective voltage stresses have not changed.

The current waveforms of the power devices within one switching cycle in ZSL-H6 and IZSL-H6 are shown in Fig. 5. It can be observed that the current amplitude of high-frequency main switches S_5 and S_6 in ZSL-H6 is $I_{La}+I_L>2I_L$, which increases the conduction loss. In contrast, the current amplitudes of the main switches S_5 and S_6 in IZSL-H6 are equal to the output current amplitude I_L, and the maximum current of all power devices does not exceed the amplitude I_{La} of the resonant current. During the turn-OFF phase of the main switches S_5 and S_6, the output current flows through the freewheeling diodes D_{f1} and D_{f2} in IZSL-H6. However, in ZSL-H6, the output current not only flows through D_{f1} and D_{f2} but also through the auxiliary switches S_{5a} and S_{6a}, resulting in an inevitable increase in conduction loss. A quantitative comparison of the conduction loss will be presented in subsequent research analyses.

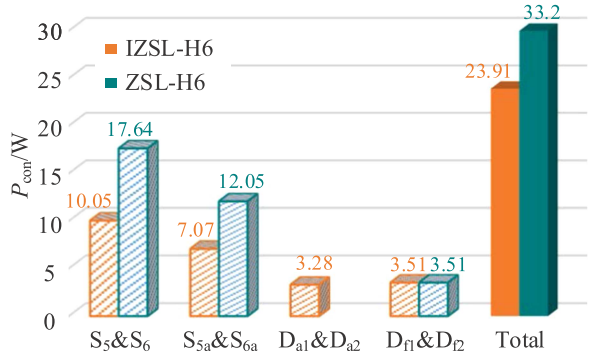

Fig. 6. Conduction loss of high-frequency semiconductor power devices of ZSL-H6 and proposed IZSL-H6.

C. Conduction Loss of High-Frequency Power Devices

To quantitatively compare the conduction loss between ZSL-H6 and IZSL-H6, the conduction loss of the high-frequency power devices was calculated while disregarding the low-frequency switches S_1–S_4 operating in the same mode. Based on the current waveform, as shown in Fig. 2(c), calculate the results according to (9), as shown in Fig. 6. The results clearly demonstrate that IZSL-H6 exhibits lower overall conduction loss compared with ZSL-H6

$$P_{con\_S5} = I_{S5\_rms}^2 R_{on} = \frac{1}{\pi}\int_0^{\pi}\left[\frac{1}{T_s}\int_{t_0}^{t_s} i_{S5}(t)dt\right]dtR_{on}. \tag{9}$$

IV. PERFORMANCE ANALYSIS

A. Parameters Design of Resonance Tank and Soft-Switching Criteria

Based on the analysis of operation principles in Section II, the following are detailed design guidelines for the parameters design of the resonance tank.

1) *Value range of L_r and C_r:* Under the constraint of resonant current, once the main switches S_5 and S_6 are turned ON, their current rises with a constant slope to achieve ZCS turn-ON. Before turning OFF S_5 and S_6, it is necessary to turn ON the auxiliary switches S_{5a} and S_{6a} to activate the resonance tanks. It facilitates the transfer of the current flowing through S_5 and S_6 to the resonance tanks, ultimately enabling the ZCS turn-OFF of S_5 and S_6. Therefore, it is a requirement that the amplitude I_{La} of the resonant current should be greater than the amplitude I_L of the output current

$$I_{La} = \frac{U_{PV}}{2Z_r} = \frac{U_{PV}}{2\sqrt{L_r/C_r}} > I_L. \tag{10}$$

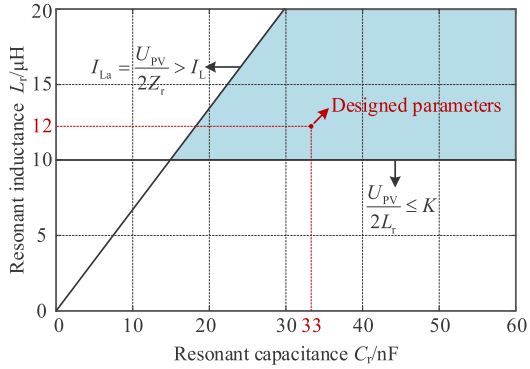

Fig. 7. Design of resonant parameters in IZSL-H6.

According to (2), the current of the main switches is constrained by the resonant inductance L_r. The rate of current rise K is associated with the rated power of the power device. Typically, K is less than 40 A/μs, and with a 100% margin considered, K is set to 20 A/μs

$$\frac{U_{\mathrm{PV}}}{2L_r}\le K. \tag{11}$$

Under the constraints of (10) and (11), suitable resonant parameters for IZSL-H6 can be chosen within the shaded region in Fig. 7.

2) *Design consideration of L_r:* The resonant inductance L_r determines the rate of current rise. A larger L_r will increase the length of the interval $[t_0, t_1]$, thereby raising the losses in the resonant tank. Therefore, based on the range of resonant parameters obtained in Step 1, choose a smaller inductance, preferably 10 μH. Considering inevitable errors in inductor winding, with a margin of 20%, L_r is selected as 12 μH.

3) *Design consideration of C_r:* After determining L_r in Step 2, it can be inferred that considering a margin for L_r will reduce the resonant current amplitude according to (10). Due to the inevitable parasitic parameters in the circuit, the actual resonant current amplitude is smaller than the theoretical value. To ensure that the resonant current amplitude is greater than the output current, it is necessary to provide an additional margin for C_r. Therefore, a resonant capacitor of 33 nF is selected.

Referring to Fig. 2(c), it can be seen that the auxiliary switches flow current within the interval $[t_2, t_3]$, covering half of the resonance period T_r. Therefore, the conduction time d_aT_s of the auxiliary switches must exceed $0.5T_r$ to ensure a ZCS turn-OFF. In the normal operation of IZSL-H6, the turn-OFF of the auxiliary switches should not occur after the turn-OFF of the main switches. The turn-OFF of the main switches within the interval $[t_4, t_6]$ is a prerequisite for achieving ZCS turn-OFF. To simplify control, the main switches and auxiliary switches can use the same sawtooth wave to generate a driving signal, and both can be turned OFF simultaneously, as depicted in Fig. 2(c). Therefore, the turn-OFF time of the auxiliary switches also falls within the interval $[t_4, t_6]$. In summary, the range of conduction time d_aT_s can be expressed as follows:

$$\frac{1}{2}T_r < d_aT_s < \frac{3}{4}T_r + \frac{1}{\omega_r}\arcsin\left(\frac{I_L}{I_{La}}\right) \tag{12}$$

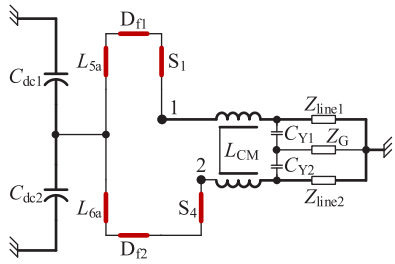

Fig. 8. CM equivalent circuit in the freewheeling-clamping mode.

TABLE III
SWITCHING STAGES, DM VOLTAGES, AND CM VOLTAGES

Switch Stage	u_{1N}	u_{2N}	u_{DM}	u_{CM}
$[t_0, t_6]$	U_{PV}	0	U_{PV}	$U_{PV}/2$
$[t_6, t_7]$	$U_{PV}/2+u_{C5a}$	$U_{PV}/2$-u_{C6a}	$2u_{C5a}$	$U_{PV}/2$
$[t_7, t_8]$	$U_{PV}/2$	$U_{PV}/2$	0	$U_{PV}/2$

where the resonant period $T_r = 2\pi\sqrt{L_rC_r}$.

The main switches and auxiliary switches can be turned OFF in the middle of the interval $[t_4, t_6]$ so that the conduction time of the auxiliary switches S_{5a} and S_{6a} can be fixed at $3T_r/4$.

B. CM Characteristic and Differential-Mode (DM) Compensation

The CM equivalent circuit in the freewheeling-clamping mode is introduced in Section II, as shown in Fig. 8. In this mode, the clamping branch is responsible for clamping the midpoints 1 and 2 of the bridge arms at a constant voltage, which can achieve a constant CM voltage and suppressing LC. Ignoring the current ripple in the output filter inductor at the switching frequency, the DM voltage u_{DM} and CM voltage u_{CM} of IZSL-H6 within one switching cycle can be represented in Table III, where $u_{\mathrm{DM}} = u_{1N}-u_{2N}$, $u_{\mathrm{CM}} = (u_{1N}+u_{2N})/2$. An important observation is that u_{CM} remains constant and u_{DM} is unipolar output.

As shown in Fig. 2(c), the operation of the resonant tank affects the DM voltage u_{DM} of IZSL-H6, causing the equivalent duty cycle of u_{DM} to deviate from sine. To eliminate this effect, compensation for the duty cycle of the main switches S_5 and S_6 is employed. Therefore, the equivalent area of the shaded part can be subtracted from the modulated wave. The calculated compensation amount can be expressed as follows:

$$\Delta d(t)=\frac{\cos^{-1}\left(\frac{i_{\mathrm{ref}}(t)}{I_{La}}\right)\sqrt{L_rC_r}+\frac{C_rU_{\mathrm{PV}}}{4i_{\mathrm{ref}}(t)}\left[1-\sqrt{1-\left(\frac{i_{\mathrm{ref}}(t)}{I_{La}}\right)^2}\right]^2}{T_s}. \tag{13}$$

V. EXPERIMENTAL RESULTS AND DISCUSSIONS

To verify the operation principle and effectiveness of the proposed IZSL-H6, a 1000-W experimental prototype was constructed in the laboratory. The prototype parameters are presented in Table IV, and the experimental setup is shown in Fig. 9.

TABLE IV
PARAMETERS OF 1000-W PROTOTYPE

Parameter	Value		
	HS-H6	ZSL-H6	IZSL-H6
Input voltage U_{PV}		400 V	
Grid voltage u_g		220 V	
Grid frequency		50 Hz	
Rated power P		1000 W	
Switching frequency f_s		50 kHz	
Power devices S_1–S_6		G3R350MT12D	
Diode D_{f1}, D_{f2}		MUR3060PT	
Filter inductance L_1, L_2		0.5 mH	
Filter capacitance C_f		2 μF	
Power devices S_{5a}, S_{6a}	/	G3R350MT12D	G3R350MT12D
Diode D_{a1}, D_{a2}	/	/	MUR3060PT
Resonant inductance L_r	/	12 μH	12 μH
Resonant capacitance C_r	/	33 nF	33 nF

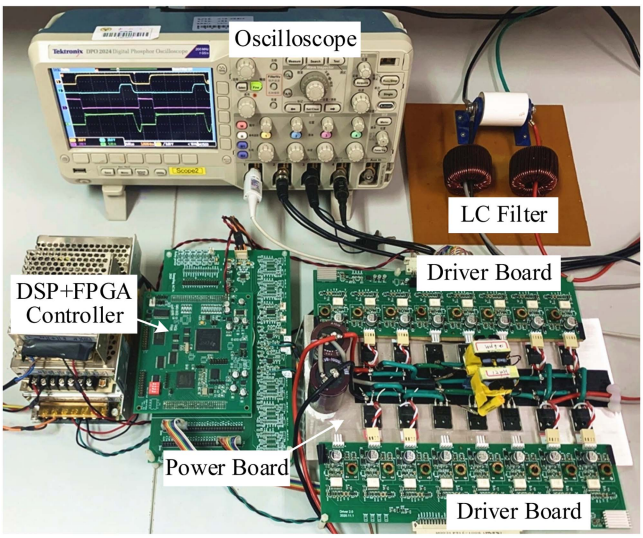

Fig. 9. Experimental setup of the IZSL-H6 inverter.

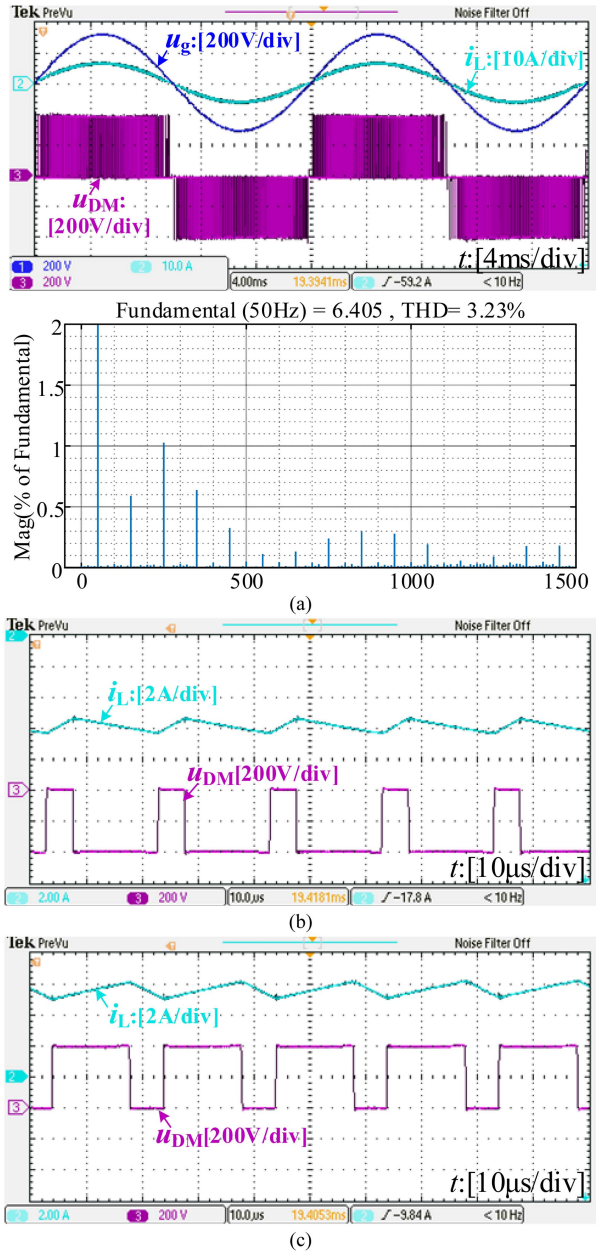

Fig. 10. Experimental waveforms of the grid voltage, the grid current, and the DM voltage. (a) DM voltage at the grid-frequency scale and FFT analysis result (u_g and u_{DM}: 200 V/div, i_L: 10 A/div, and time: 4 ms/div). (b) DM voltage in the positive half-cycle at the switching-frequency scale (i_L: 2 A/div, time: 10 μs/div). (c) DM voltage in the negative half-cycle at the switching-frequency scale.

A. Verification of the DM Performance

The DM characteristics of IZSL-H6 under rated power are shown in Fig. 10. In Fig. 10(a), the experimental waveforms of grid voltage u_g, output current i_L, and DM voltage u_{DM} are shown on the grid-frequency scale. It can be observed that the DM voltage exhibits unipolar output characteristics. Fig. 10(b) and (c) represents the experimental waveforms of i_L and u_{DM} at the switching-frequency scale in the positive and negative half-cycles of the grid, respectively.

B. Verification of the CM Performance

Fig. 11 illustrates the experimental waveforms of CM characteristics of IZSL-H6 under rated power. Fig. 11(a) shows the experimental waveforms of grid voltage u_g, output current i_L, voltage u_{1N}, and voltage u_{2N} at the grid-frequency scale. The waveforms at the switching-frequency scale in the positive and negative half-cycles are depicted in Fig. 11(b) and (c), respectively. From $2u_{CM} = u_{1N}+u_{2N}$, it can be observed that IZSL-H6 has a constant CM voltage, which is consistent with the theoretical analysis in Section III-B. Therefore, IZSL-H6 has an excellent LC suppression function.

C. Verification of the Soft-Switching Performance

Fig. 12 shows the experimental waveforms of the gate driving voltage u_{GS5}, u_{GS5a}, resonant voltage u_{C5a}, and resonant current i_{L5a}. It can be observed that the resonance tank operates normally when S_{5a} is turned ON, and the amplitude of the voltage u_{C5a} is equal to the input voltage U_{PV}. The experimental results validate the principal analysis, as presented in Fig. 2(c).

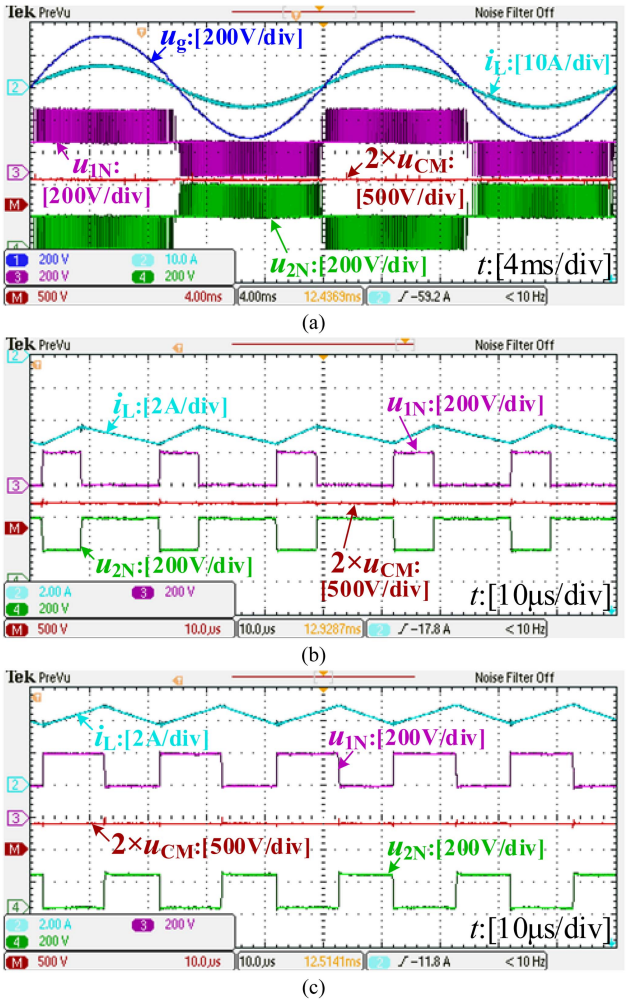

Fig. 11. Experimental waveforms of the grid voltage, the grid current, and the CM voltage. (a) DM voltage at the grid-frequency scale (u_g and $u_{\rm CM}$: 200 V/div, i_L: 10 A/div, and time: 4 ms/div). (b) CM voltage in the positive half-cycle at the switching-frequency scale (i_L: 2 A/div, time: 10 μs/div). (c) CM voltage in the negative half-cycle at the switching-frequency scale.

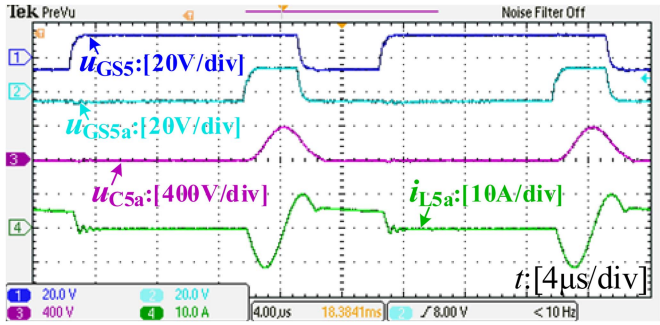

Fig. 12. Experimental waveform of resonant voltage and resonant current (u_{GS5} and u_{GS5a}: 20 V/div, u_{C5a}: 400 V/div, i_{L5a}: 10 A/div, and time: 4 μs/div).

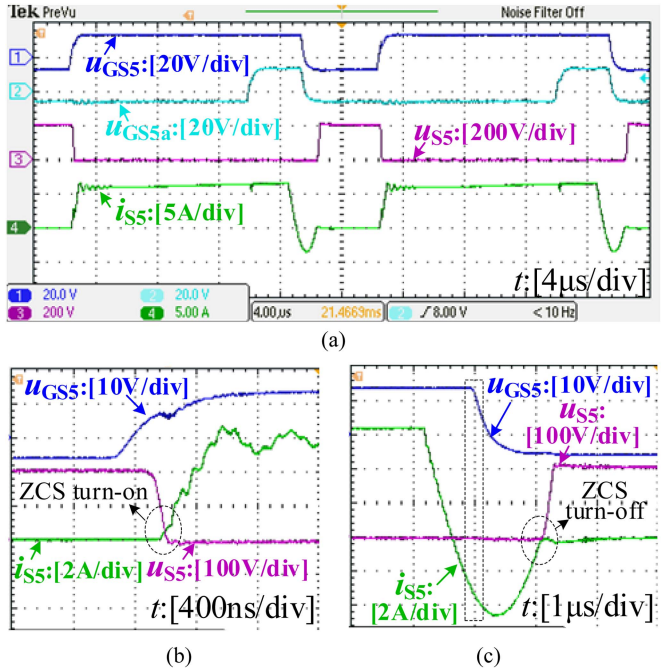

Fig. 13. Experimental waveforms of high-frequency main switch S_5. (a) Voltage and current waveforms of S_5 at switching cycle (u_{GS5} and u_{GS5a}: 20 V/div, u_{S5}: 200 V/div, i_{S5}: 5 A/div, and time: 4 μs/div). (b) S_5 achieves ZCS turn-ON (u_{GS5}: 10 V/div, u_{S5}: 100 V/div, i_{S5}: 2 A/div, and time: 400 ns/div). (c) S_5 achieves ZCS turn-OFF (u_{GS5}: 10 V/div, u_{S5}: 100 V/div, i_{S5}: 2 A/div, and time: 1 μs/div).

The experimental waveforms of u_{GS5}, u_{GS5a}, voltage u_{S5}, and current i_{S5} of S_5 at switching cycle are shown in Fig. 13(a). The current i_{S5} linearly increases after S_5 is turned ON, achieving ZCS turn-ON for S_5, as shown in Fig. 13(b). After the current i_{S5} rises, there is no superposition of the sine resonant current, and it remains approximately constant. It means that only the output current flows through S_5. Fig. 13(c) shows that when the turn-OFF signal arrives, i_{S5} is already negative, thus achieving ZCS turn-OFF for S_5. In addition, the voltage stress u_{S5} is $U_{\rm PV}/2$.

The experimental waveforms of u_{GS5}, u_{GS5a}, voltage u_{S5a}, and current i_{S5a} of S_{5a} at switching cycle are shown in Fig. 14(a). Switch S_{5a} achieves ZCS turn-ON and turn-OFF due to carrying the resonant current of half a resonant cycle, as shown in Fig. 14(b) and (c). Because of the resonance action between the resonant inductor and the parasitic capacitor of the power device, a voltage spike appears in the voltage u_{S5a} during the switching state, and the voltage amplitude does not exceed the input voltage $U_{\rm PV}$. After reaching stability, u_{S5a} stabilized at $U_{\rm PV}/2$. Fig. 15(a) shows the voltage and current waveforms of u_{GS5}, u_{GS5a}, voltage u_{Da1}, and current i_{Da1} of D_{a1} at switching cycle. After the current i_{Da1} drops to zero, the voltage u_{Da1} remains at zero, achieving ZCS turn-OFF for D_{a1} and significantly mitigating the reverse recovery issue, as shown in Fig. 15(b).

The experimental waveforms of u_{GS5}, u_{GS5a}, the voltage u_{Df1}, and the current i_{Df1} of the freewheeling diode D_{f1} are shown in Fig. 16(a). Fig. 16(b) shows that the current i_{Df1} decreases linearly to zero, enabling D_{f1} to achieve ZCS turn-OFF and effectively mitigating the reverse recovery issue.

D. Verification of the Dynamic Performance

The dynamic response waveforms of the IZSL-H6 inverter are shown in Fig. 17 when the output current i_L rises and drops

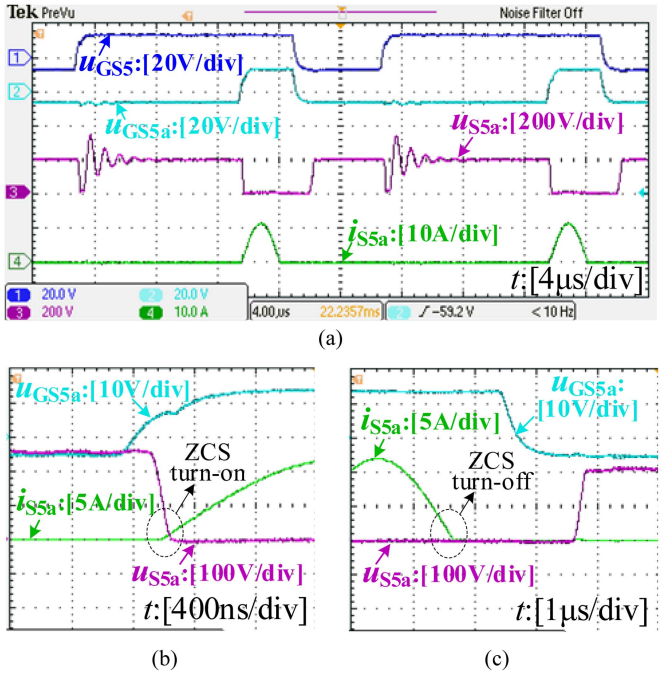

Fig. 14. Experimental waveforms of auxiliary switch S_{5a}. (a) Voltage and current waveforms of S_{5a} at switching cycle (u_{GS5} and u_{GS5a}: 20 V/div, u_{S5a}: 200 V/div, i_{S5a}: 10 A/div, and time: 4 μs/div), (b) S_{5a} achieves ZCS turn-ON (u_{GS5a}: 10 V/div, u_{S5a}: 100 V/div, i_{S5a}: 5 A/div, and time: 400 ns/div). (c) S_{5a} achieves ZCS turn-OFF (u_{GS5a}: 10 V/div, u_{S5a}: 100 V/div, i_{S5a}: 5 A/div, and time: 1 μs/div).

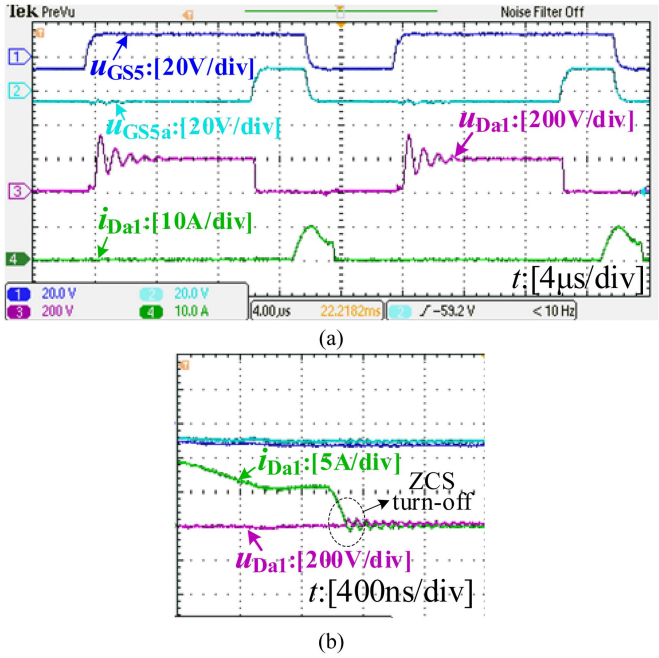

Fig. 15. Experimental waveforms of auxiliary diode D_{a1}. (a) Voltage and current waveforms of S_{5a} (u_{GS5} and u_{GS5a}: 20 V/div, u_{Da1}: 200 V/div, i_{Da1}: 10 A/div, and time: 4 μs/div). (b) D_{a1} achieves ZCS turn-OFF (u_{Da1}: 100 V/div, i_{Da1}: 5 A/div, and time: 400 ns/div).

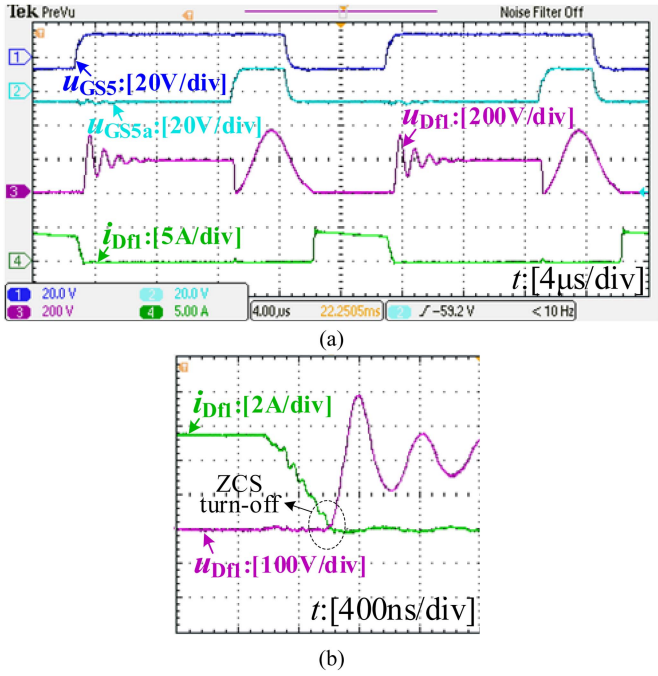

Fig. 16. Experimental waveforms of freewheeling diode D_{f1}. (a) Voltage and current waveforms of D_{f1} (u_{GS5} and u_{GS5a}: 20 V/div, u_{Df1}: 200 V/div, i_{Df1}: 5 A/div, and time: 4 μs/div). (b) D_{f1} achieves ZCS turn-OFF (u_{Df1}: 100 V/div, i_{Df1}: 2 A/div, and time: 400 ns/div).

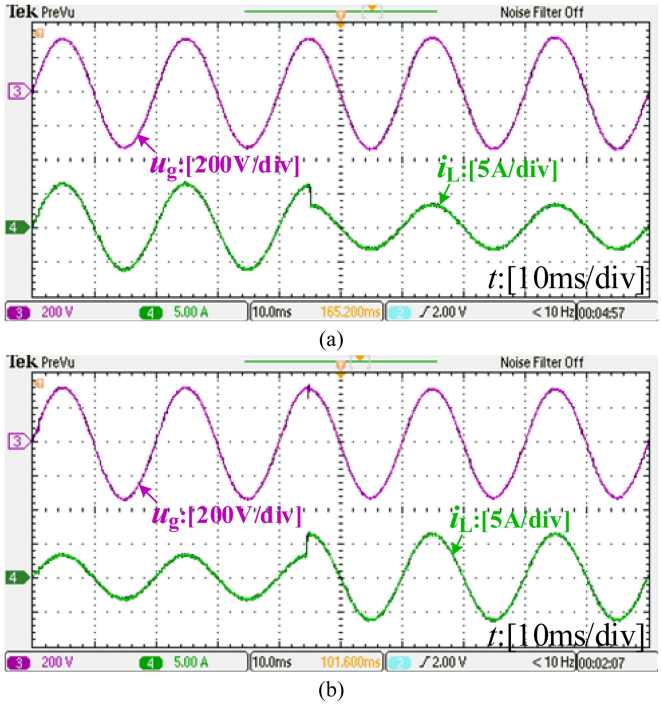

Fig. 17. Dynamic response of output current i_L. (a) i_L drops from full-load to half-load (u_g: 200 V/div, i_L: 5 A/div, and time: 4 ms/div). (b) i_L rises from half-load to full-load.

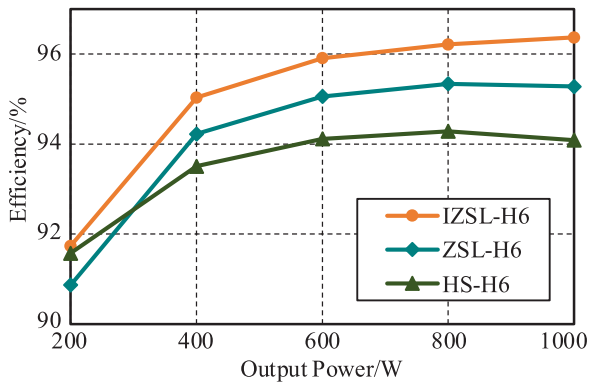

Fig. 18. Efficiency curves comparison among the IZSL-H6, ZSL-H6 [35], and HS-H6 [17].

suddenly. It can be seen that during the sudden switch between full-load and half-load, IZSL-H6 represents good dynamic response performance, as shown in Fig. 17(a) and (b).

Fig. 18 illustrates the efficiency curves comparison among HS-H6, IZSL-H6, and ZSL-H6 at different output powers to validate the efficiency advantages of the proposed IZSL-H6. It can be observed that the efficiency of IZSL-H6 and HS-H6 is similar and slightly higher than ZSL-H6 when the output power is 200 W. As the output power increases, the efficiency of IZSL-H6 and ZSL-H6 is higher than HS-H6. The efficiency of IZSL-H6 at full-load is 96.37%, which is 1.09% higher than ZSL-H6. In summary, within the full power range, the efficiency of IZSL-H6 is higher than ZSL-H6.

VI. Conclusion

An improved ZSL inverter with low conduction loss has been proposed in this article. Several clear merits are summarized as follows.

1) All power devices in the proposed IZSL-H6 feature zero-current turn-ON and turn-OFF, achieving ZSL and eliminating diode reverse recovery issues.
2) The excellent LC suppression performance of IZSL-H6 has been demonstrated, as the CM voltage remains constant under unipolar SPWM control.
3) The resonance tanks and the main power loops are separated in the proposed IZSL-H6. Compared with ZSL-H6, the current amplitude of the main switches in IZSL-H6 is reduced to the output current from twice the output current. In addition, IZSL-H6 reduces the number of power devices through which resonant current flows and reduces conduction loss.

These advantages were validated through experimentation with a 1000-W IZSL-H6 prototype. The results indicate that the proposed improved ZSL inverter is suitable for transformerless PV generation systems.

References

[1] F. Blaabjerg, R. Teodorescu, M. Liserre, and A. V. Timbus, "Overview of control and grid synchronization for distributed power generation systems," *IEEE Trans. Ind. Electron.*, vol. 53, no. 5, pp. 1398–1409, Oct. 2006.
[2] J. M. Carrasco et al., "Power-electronic systems for the grid integration of renewable energy sources: A survey," *IEEE Trans. Ind. Electron.*, vol. 53, no. 4, pp. 1002–1016, Jun. 2006.
[3] Y. Tang, W. Yao, P. C. Loh, and F. Blaabjerg, "Highly reliable transformerless photovoltaic inverters with leakage current and pulsating power elimination," *IEEE Trans. Ind. Electron.*, vol. 63, no. 2, pp. 1016–1026, Feb. 2016.
[4] J. T. Stauth, M. D. Seeman, and K. Kesarwani, "Resonant switched-capacitor converters for sub-module distributed photovoltaic power management," *IEEE Trans. Power Electron.*, vol. 28, no. 3, pp. 1189–1198, Mar. 2013.
[5] P. Jain, J. Poon, J. P. Singh, C. Spanos, S. R. Sanders, and S. K. Panda, "A digital twin approach for fault diagnosis in distributed photovoltaic systems," *IEEE Trans. Power Electron.*, vol. 35, no. 1, pp. 940–956, Jan. 2020.
[6] T. Kerekes, R. Teodorescu, and M. Liserre, "Common mode voltage in case of transformerless PV inverters connected to the grid," in *Proc. IEEE Int. Symp. Ind. Electron.*, 2008, pp. 2390–2395.
[7] Y. Gu, W. Li, Y. Zhao, B. Yang, C. Li, and X. He, "Transformerless inverter with virtual DC bus concept for cost-effective grid-connected PV power systems," *IEEE Trans. Power Electron.*, vol. 28, no. 2, pp. 793–805, Feb. 2013.
[8] N. V. Kurdkandi et al., "A new transformer-less common grounded three-level grid-tied inverter with voltage boosting capability," *IEEE Trans. Energy Convers.*, vol. 36, no. 3, pp. 1896–1909, Sep. 2021.
[9] J. M. A. Myrzik and M. Calais, "String and module integrated inverters for single-phase grid connected photovoltaic systems—A review," in *Proc. IEEE Bologna Power Tech Conf. Proc.*, 2003, pp. 430–437.
[10] L. Zhou, F. Gao, and T. Xu, "Implementation of active NPC circuits in transformer-less single-phase inverter with low leakage current," *IEEE Trans. Ind. Appl.*, vol. 53, no. 6, pp. 5658–5667, Nov. 2017.
[11] B. Yang, W. Li, Y. Gu, W. Cui, and X. He, "Improved transformerless inverter with common-mode leakage current elimination for a photovoltaic grid-connected power system," *IEEE Trans. Power Electron.*, vol. 27, no. 2, pp. 752–762, Feb. 2012.
[12] M. Victor et al., "Method of converting a direct current voltage from a source of direct current voltage, more specifically from a photovoltaic source of direct current voltage, into a alternating current voltage," U.S. Patent US7411802B2, Aug. 12, 2008.
[13] H. Schmidt, C. Siedle, and J. Ketterer, "Wechselrichter zum unwandeln einer elektrischen gleichspannung in einen wechselstrom oder eine wechselspannung," U.S. Patent DE50311515D1, 2003.
[14] M. Islam and S. Mekhilef, "H6-type transformerless single-phase inverter for grid-tied photovoltaic system," *IET Power Electron.*, vol. 8, no. 4, pp. 636–644, Apr. 2015.
[15] H. Xiao and S. Xie, "Leakage current analytical model and application in single-phase transformerless photovoltaic grid-connected inverter," *IEEE Trans. Electromagn. Compat.*, vol. 52, no. 4, pp. 902–913, Nov. 2010.
[16] T. K. S. Freddy, N. A. Rahim, W.-P. Hew, and H. S. Che, "Comparison and analysis of single-phase transformerless grid-connected PV inverters," *IEEE Trans. Power Electron.*, vol. 29, no. 10, pp. 5358–5369, Oct. 2014.
[17] R. Gonzalez, J. Lopez, P. Sanchis, and L. Marroyo, "Transformerless inverter for single-phase photovoltaic systems," *IEEE Trans. Power Electron.*, vol. 22, no. 2, pp. 693–697, Mar. 2007.
[18] L. Zhang, K. Sun, L. Feng, H. Wu, and Y. Xing, "A family of neutral point clamped full-bridge topologies for transformerless photovoltaic grid-tied inverters," *IEEE Trans. Power Electron.*, vol. 28, no. 2, pp. 730–739, Feb. 2013.
[19] H. Xiao, S. Xie, Y. Chen, and R. Huang, "An optimized transformerless photovoltaic grid-connected inverter," *IEEE Trans. Ind. Electron.*, vol. 58, no. 5, pp. 1887–1895, May 2011.
[20] Z. Ahmad and S. N. Singh, "An improved single phase transformerless inverter topology for grid connected PV system with reduce leakage current and reactive power capability," *Sol. Energy*, vol. 157, pp. 133–146, Nov. 2017.
[21] Y. Mei, S. Hu, L. Lin, W. Li, X. He, and F. Cao, "Highly efficient and reliable inverter concept-based transformerless photovoltaic inverters with tri-direction clamping cell for leakage current elimination," *IET Power Electron.*, vol. 9, no. 8, pp. 1675–1683, Jun. 2016.
[22] R. Li and D. Xu, "A zero-voltage switching three-phase inverter," *IEEE Trans. Power Electron.*, vol. 29, no. 3, pp. 1200–1210, Mar. 2014.
[23] N. Sukesh, M. Pahlevaninezhad, and P. K. Jain, "Analysis and implementation of a single-stage flyback PV microinverter with soft switching," *IEEE Trans. Ind. Electron.*, vol. 61, no. 4, pp. 1819–1833, Apr. 2014.

[24] D. M. Divan and G. Skibinski, "Zero-switching-loss inverters for high-power applications," *IEEE Trans. Ind. Appl.*, vol. 25, no. 4, pp. 634–643, Aug. 1989.
[25] D. M. Divan, "The resonant DC link converter—A new concept in static power conversion," *IEEE Trans. Ind. Appl.*, vol. 25, no. 2, pp. 317–325, Apr. 1989.
[26] J. G. Cho, H. S. Kim, and G. H. Cho, "Novel soft switching PWM converter using a new parallel resonant DC-link," in *Proc. Rec. IEEE 22nd Annu. Power Electron. Specialists Conf.*, 1991, pp. 241–247.
[27] B. Kou, J. Wei, and L. Zhang, "Switching and conduction loss reduction of dual-buck full-bridge inverter through ZVT soft-switching under full-cycle modulation," *IEEE Trans. Power Electron.*, vol. 35, no. 5, pp. 5031–5046, May 2020.
[28] Y. Chen and D. Xu, "Pulse-width modulation scheme for a ZVS single-phase inverter in rectifier operation," in *Proc. IEEE Appl. Power Electron. Conf. Expo.*, 2018, pp. 2488–2495.
[29] R. Gurunathan and A. K. S. Bhat, "Zero-voltage switching DC link single-phase pulsewidth-modulated voltage source inverter," *IEEE Trans. Power Electron.*, vol. 22, no. 5, pp. 1610–1618, Sep. 2007.
[30] Y. Chen et al., "A ZVS grid-connected full-bridge inverter with a novel ZVS SPWM scheme," *IEEE Trans. Power Electron.*, vol. 31, no. 5, pp. 3626–3638, May 2016.
[31] M. Hazrati-Karkaragh, M. Esteki, M. R. Mohammadi, and S. A. Khajehoddin, "A novel high-frequency inverter with ZVT in a wide range of duty cycles and PFs," *IEEE Trans. Power Electron.*, vol. 38, no. 8, pp. 9983–9997, Aug. 2023.
[32] Y. Xia and R. Ayyanar, "Naturally adaptive, low-loss zero-voltage-transition circuit for high-frequency full-bridge inverters with hybrid PWM," *IEEE Trans. Power Electron.*, vol. 33, no. 6, pp. 4916–4933, Jun. 2018.
[33] H. Xiao, X. Liu, and K. Lan, "Zero-voltage-transition full-bridge topologies for transformerless photovoltaic grid-connected inverter," *IEEE Trans. Ind. Electron.*, vol. 61, no. 10, pp. 5393–5401, Oct. 2014.
[34] H. Xiao, K. Lan, B. Zhou, L. Zhang, and Z. Wu, "A family of zero-current-transition transformerless photovoltaic grid-connected inverter," *IEEE Trans. Power Electron.*, vol. 30, no. 6, pp. 3156–3165, Jun. 2015.
[35] H. Xiao, L. Zhang, Z. Wang, and M. Cheng, "A new soft-switching configuration and its application in transformerless photovoltaic grid-connected inverters," *IEEE Trans. Ind. Electron.*, vol. 65, no. 12, pp. 9518–9527, Dec. 2018.

Yun Liu was born in Henan Province, China. She received the B.S. and M.S. degrees in automation from the Qingdao University of Technology, Qingdao, China, in 2017 and 2020, respectively. She is currently working toward the Ph.D. degree in electrical engineering with Southeast University, Nanjing, China.

Her research interests include high-frequency high-power density inverter and soft-switching technology.

Huafeng Xiao (Senior Member, IEEE) was born in Hubei Province, China. He received the B.S., M.S., and Ph.D. degrees in electrical engineering from the Nanjing University of Aeronautics and Astronautics, Nanjing, China, in 2004, 2007, and 2010, respectively.

In 2011, he joined the Faculty of Power Electronics and is currently a Professor with the College of Electrical Engineering, Southeast University, Nanjing, China. From 2015 to 2016, he was a Postdoctoral Fellow with the Department of Electrical and Computer Engineering, Ryerson University, Toronto, ON, Canada. From 2016 to 2017, he was a Postdoctoral Fellow with the Department of Electrical and Computer Engineering, McGill University, Montreal, QC, Canada. His research interests include transformerless photovoltaic power systems and high-frequency soft-switching conversions. He has authored more than 100 technical papers in Journals and Conference proceedings, and held 50 China patents and one U.S. patent, and authored three books as well.

Wei Hua (Senior Member, IEEE) received the B.Sc. and Ph.D. degrees in electrical engineering from Southeast University, Nanjing, China, in 2001 and 2007, respectively.

From 2004 to 2005, he was with the Department of Electronics and Electrical Engineering, University of Sheffield, U.K., as a Joint-Supervised Ph.D. Student. Since 2007, he has been with Southeast University, where he is currently a Chief Professor with Southeast University and a Distinguished Professor in Jiangsu Province. He has coauthored more than 150 technical papers. He holds 50 patents in his areas of interest. His teaching and research interests include the design, analysis, and control of electrical machines, especially for PM brushless machines and switching reluctance machines, etc.

Ming Cheng (Fellow, IEEE) received the B.Sc. and M.Sc. degrees from the Department of Electrical Engineering, Southeast University, Nanjing, China, in 1982 and 1987, respectively, and the Ph.D. degree from the Department of Electrical and Electronic Engineering, The University of Hong Kong, Hong Kong, in 2001, all in electrical engineering.

Since 1987, he has been with Southeast University, where he is currently a Chair Professor with the School of Electrical Engineering and the Director of the Research Center for Wind Power Generation. From January to April 2011, he was a Visiting Professor with Wisconsin Electric Machine and Power Electronics Consortium, University of Wisconsin-Madison, Madison, WI, USA. His teaching and research interests include electrical machines, motor drives for electric vehicles, and renewable energy generation. He has authored or coauthored more than 360 technical papers and four books and is the holder of 100 patents in these areas.

Dr. Cheng is a fellow of the Institution of Engineering and Technology. He has served as the Chair and organizing committee member for many international conferences. He is a Distinguished Lecturer of the IEEE Industry Applications Society in 2015 and 2016.